1 **Moment Tensor Estimation of Event S1222a and Implications for Tectonics Near the**
2 **Dichotomy Boundary in Southern Elysium Planitia, Mars**

3 **R. Maguire[1*], V. Lekic[2], D. Kim[3], N. Schmerr[2], J. Li[4], C. Beghein[4], Q. Huang[5], J. C. E.**
4 **Irving[6], F. Karakostas[2,7], P. Lognonné[8], S. C. Stähler [3], W. B. Banerdt[9]**

5

6 [1]Department of Earth Science and Environmental Change, University of Illinois Urbana-
7 Champaign, Champaign, IL, USA.

8 [2]Department of Geology, University of Maryland, College Park, MD,USA.

9 [3]Institute of Geophysics, ETH Zürich, Zürich, Switzerland.

10 [4]Department of Earth, Planetary, and Space Sciences, University of California, Los Angeles, Los
11 Angeles, CA, USA.

12 [5]Department of Geophysics, Colorado School of Mines, Golden, CO, USA.

13 [6]School of Earth Sciences, University of Bristol, Bristol, UK.

14 [7]Istituto Nazionale di Geofisica e Vulcanologia, Bologna, Italy

15 [8]Institut de Physique du Globe de Paris, Université de Paris, CNRS, Paris, France.

16 [9]Jet Propulsion Laboratory, California Institute of Technology, Pasadena, CA, USA.

17

18 Corresponding author: Ross Maguire (rossrm@illinois.edu)

19 **Key Points:**

20 - We performed a moment tensor inversion of S1222a based on waveform fitting of both
21   body and surface waves.

22 - The scalar moment of S1222a is between $3.5\times10^{15} - 5.0\times10^{15}$ Nm.

23 - S1222a likely resulted from dip slip faulting in the crust on an E-W to SE-NW striking
24   fault plane.

Abstract

25

26   On May 4th, 2022 the InSight seismometer SEIS recorded the largest marsquake ever observed,
27   S1222a, with an initial magnitude estimate of Mw 4.7. Understanding the depth and source
28   properties of this event has important implications for the nature of tectonic activity on Mars.
29   Located ~37 degrees to the southeast of InSight, S1222a is one of the few non-impact
30   marsquakes that exhibits prominent ratio surface waves. We use waveform modeling of body
31   waves (P and S) and surface waves (Rayleigh and Love) to constrain the moment tensor and
32   quantify the associated uncertainty. We find that S1222a likely resulted from dip-slip faulting in
33   the mid-crust (source depth ~18 – 28 km) and estimate a scalar moment of $3.5 \times 10^{15} - 5.0 \times 10^{15}$
34   Nm (magnitude Mw 4.3 – 4.4). The best-fitting focal mechanism is sensitive to the choice of
35   phase windows and misfit weights, as well as the structural model of Mars used to calculate
36   Green's functions. We find that an E-W to SE-NW striking thrust fault can explain the data well,
37   although depending on the choice of misfit weighting, a normal fault solution is also permissible.
38   The orientation of the best-fitting fault plane solutions suggests that S1222a takes place on a
39   fault system near the martian crustal dichotomy accommodating relative motion between the
40   northern lowlands and southern highlands. Independent constraints on the event depth and
41   improved models of the (an)isotropic velocity structure of the martian crust and mantle could
42   help resolve the ambiguity inherent to single-station moment tensor inversions of S1222a and
43   other marsquakes.
44

Plain Language Summary

45

46   The InSight lander's sensitive seismometer recorded over 1,000 marsquakes during the course of
47   its mission. Like the Earth, it is thought that the majority of quakes on Mars result from faulting
48   events that release stress within the planetary interior. Understanding the nature of these events,
49   including their magnitude, depth, and faulting style provides valuable clues into planetary
50   deformation and its driving forces. In this study, we use seismic waveform modeling to constrain
51   the properties of the S1222a event, the largest marsquake recorded during the InSight mission.
52   We find that S1222a likely resulted from faulting within the crust of Mars, and estimate the
53   event was equivalent to a 4.3 – 4.4 magnitude event on Earth. Our analysis places constraints on
54   the geometry of the fault plane, although it is difficult to conclusively determine if S1222a
55   resulted from compressional or extensional forces. The ambiguity arises from the sensitivity of
56   the analysis to subjective parameter choices. Further advances may be possible if more accurate
57   models of the interior structure of Mars become available.

1 Introduction

58

59   Seismic moment tensors provide key insights into the orientation of active faults, slip across
60   faults, and the distribution of stress in planetary interiors. On Earth, moment tensors are routinely
61   calculated following significant seismic events (e.g. Dziewonski and Woodhouse, 1983) and
62   have played a crucial role in understanding global patterns of seismicity as well as deformation
63   across tectonic settings (e.g., Ekström et al., 2012). Techniques to constrain source
64   characteristics of teleseismic events typically rely on data from globally distributed seismic
65   stations, and optimal focal mechanisms are found either by fitting body wave first motions (e.g.
66   Brumbaugh, 1979) or by fitting waveforms of intermediate period body wave (Langston and
67   Helmberger, 1975) or surface wave phases (e.g. Arvidsson and Ekstrom, 1998), or complete long
68   period waveforms (e.g. Dziewonski et al. 1981). Information about source depth comes from the

69 lag-time of depth phases (e.g. Basham and Ellis, 1969) and/or by the frequency dependence of
70 surface wave excitation (e.g. Tsai and Aki, 1970).
71
72 On Mars, moment tensor inversions are challenging for three reasons: 1) only a single seismic
73 station is available, limiting the sampling of the focal sphere; 2) depth phases are only rarely
74 unequivocally identified rendering source depth estimates inaccurate; and, 3) contribution of
75 along-path structure to waveforms is difficult to estimate due to unknown three-dimensional
76 (3D) structure. However, since different seismic phases have different radiation patterns and
77 sample different portions of the focal sphere, single station moment tensor inversions are
78 possible for sufficiently high-quality events, provided that sufficiently accurate structural models
79 are available.
80
81 After more than two martian years on the surface, the InSight (Interior Exploration using Seismic
82 Investigations, Geodesy, and Heat Transport, Banerdt et al. 2020) lander and associated
83 seismometer (Lognonné et al., 2019) has helped transform our understanding of the interior and
84 dynamics of Mars. InSight landed in the Elysium Planitia of Mars on November 16, 2018 and
85 has recorded over 1,000 marsquakes (Ceylan et al., 2022) with distinct spectral characteristics
86 (e.g. Giardini et al. 2020), revealing seismo-tectonically active zones (e.g., Stähler et al., 2022).
87 The majority of the observed marsquakes are low-magnitude high frequency (HF) events with
88 energy above 2.4 Hz, which have been interpreted as having crustal propagation paths and have
89 helped determine the physical properties of the shallow subsurface (Lognonné et al., 2020;
90 Karakostas et al., 2021; Menina et al., 2021). Although larger low-frequency (LF) and broadband
91 (BB) marsquakes with mantle traversing paths are less commonly observed, these events have
92 been key for constraining the deep interior structure of Mars, including crustal structure below
93 (Knapmeyer-Endrun et al., 2021; Kim et al., 2021a; Li et al., 2022a; Durán et al., 2022a) and
94 away (Kim et al. 2022a, 2022b; Li et al. 2022c, 2022d) from InSight, crustal anisotropy (Beghein
95 et al. 2022; Kim et al. 2022b; Li et al. 2022b), upper mantle seismic wave speed (Khan et al.,
96 2021; Durán 2022b), the radius of the core (Stähler et al., 2021; Khan et al., 2022, Durán et al.,
97 2022a), and mineral phase transitions in the deep mantle (Huang et al., 2022).
98
99 Prior to the arrival of InSight on Mars, reverse faulting due to planetary contraction driven by
100 secular cooling was expected to be one of the principal drivers of seismicity (Solomon et al.,
101 1991). Thus far, however, seismic evidence of ongoing tectonic activity has come from the
102 Cerberus Fossae extensional graben system which has been a prominent source of both HF and
103 LF marsquakes (Stähler et al., 2022). Moment tensor estimates based on detailed waveform
104 fitting of body waves from Cerberus Fossae events S0173a and S0235b implied extension along
105 steeply dipping normal faults with roughly E-W strike orientations (Brinkman et al., 2021).
106 Alternatively, based on body wave polarities and relative amplitudes, Sita & van der Lee (2022)
107 found that S0173a can be best fit as a marsquake doublet that starts as a thrust followed by
108 oblique normal faulting. They also found that S0235b likely represents vertical dip-slip motion
109 with a small normal faulting component. Recently, Jacob et al., (2022) estimated moment tensor
110 solutions from nine high-quality LF and broadband (BB) marsquakes located in Cerberus Fossae
111 and surrounding regions using P and S waveform fits, secondary phase amplitudes, and a lack of
112 surface wave detection criteria. They found that two of the events (S0325a and S0784a) located
113 south of Cerberus Fossae near the martian crustal dichotomy boundary are consistent with thrust

114 faulting source mechanisms. Additionally, they located the hypocenters of all nine tectonic
115 events to moderate depths in the crust (15 – 36 km).
116
117 On May 4th, 2022, InSight recorded the seismic event S1222a, the largest marsquake observed
118 during the mission, with an initial estimated moment magnitude of Mw 4.7 (Kawamura et al.,
119 2022). Despite occurring in the early afternoon during a period of high background noise due to
120 strong winds, InSight's very broad band seismometer, SEIS VBB (Lognonné et al., 2019),
121 recorded some of the clearest seismic waveforms of any marsquake observed during the InSight
122 mission (Fig 1). S1222a was designated a quality A event by the Mars Quake Service (MQS) due
123 to its high signal-to-noise ratio and the identification of both body and surface wave phases with
124 clear polarization (Kawamura et al., 2022). Waveform data from SEIS is archived and made
125 publicly available by the InSight Mars SEIS Data Service (InSight Mars SEIS Data Service,
126 2019). Several prominent instrument glitches are present during the event (Fig. 1D). Although
127 glitches have been shown to be capable of influencing seismic analysis and interpretation (Kim
128 et al., 2021b), no glitches are apparent near the phases of interest in this study. Importantly, both
129 Love and Rayleigh waves were identified in the waveforms of S1222a with no glitches
130 (Kawamura et al., 2022); modeling of fundamental-mode dispersion (Beghein et al., 2022)
131 together with overtones (Kim et al., 2022b) revealed substantial large-scale radial anisotropy in
132 the martian crust. The observation of Rayleigh and Love waves also provides complementary
133 constraints on the moment tensor, which have not been available to other marsquake moment
134 tensor inversions.
135
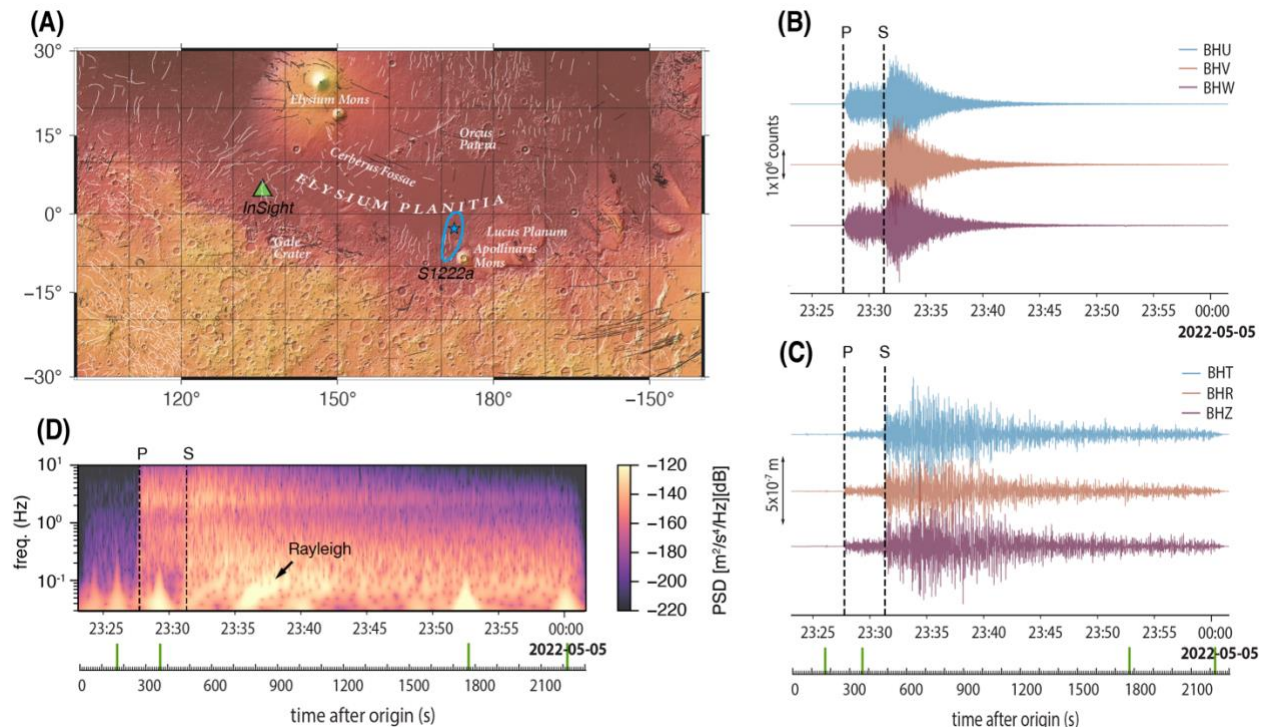
136
137 Figure 1. (A) Map showing the location of InSight (green triangle) and the MQS reported location of
138 S1222a (blue star, with uncertainty ellipse) (Kawamura et al., 2022). Thin white and black lines indicate
139 mapped compressional and extensional faults, respectively, from the database of Knapmeyer et al. (2006).
140 (B) Raw recordings of S1222a from the SEIS VBB instrument. The dashed vertical lines show the MQS
141 arrival times of P and S. (C) Same as (B) but the data is instrument corrected and rotated to vertical

142   (BHZ), radial (BHR), and transverse (BHT) components using a back azimuth of 107.7 degrees. All
143   components are bandpass filtered between 0.1 - 0.6 Hz. (D) Spectrogram of BHZ data. Vertical green
144   lines on the lower time axis mark clearly apparent instrument glitches.

145

146   In this paper, we use seismic waveforms from both body waves (P and S) and, for the first time,
147   surface waves (Rayleigh and Love) to estimate the best-fitting magnitude, depth, and focal
148   mechanism of S1222a. We take advantage of available models of the crustal structure along the
149   S1222a minor-arc paths, which were obtained by modeling the group velocity dispersion of
150   Rayleigh and Love minor arc phases (Beghein et al., 2022) and their overtones (Kim et al.
151   2022b). We outline a strategy for marsquake moment tensor inversion based on a grid search
152   approach which allows uncertainty estimation on event depth and faulting style.

2 Moment tensor inversion

154   For S1222a, the MQS reported an origin time of UTC 2022-05-04T23:23:07 (+/- 4.8 s) and an
155   epicentral distance of 37 +/- 1.6 degrees, based on the S – P differential travel times (InSight
156   Marsquake Service, 2023). Additionally, based on the P-wave polarization, the back azimuth of
157   the event was reported to be 101º, although subsequent analysis by MQS based on body wave
158   polarization attributes measured in multiple frequency bands suggested a bimodal distribution of
159   likely back azimuths, with peaks between 96º and 112º. While the discrepancies between
160   estimates of back azimuth (and therefore source location) are of geophysical interest and could
161   potentially be informative of 3D propagation effects along the path, the exceptional signal-to-
162   noise ratio and clear polarization of P strongly suggests a source location in southern Elysium
163   Planitia, northwest of Apollinaris Mons (Fig 1A).

164

165   We estimate the best-fitting moment tensor solution of S1222a by inverting waveforms of P, S,
166   Rayleigh, and Love wave phases recorded by SEIS VBB. Even though moment tensor estimation
167   is a linear inverse problem for a fixed velocity model, the determination of source depth is not.
168   Optimal phase alignment between synthetic and observed waveforms is achieved by alignment
169   based on cross-correlation, as commonly done in regional moment tensor inversions on Earth
170   (e.g. Dreger et al., 2021); this alignment introduces an additional nonlinearity into the moment
171   tensor inversion. Therefore, we choose to use a grid search approach. The synthetic waveforms
172   are computed using Instaseis (van Driel et al., 2015), which allows rapid retrieval of pre-
173   computed Green's functions based on AxiSEM waveform simulations (Nissen-Meyer et al.,
174   2014). The velocity model used to compute synthetic waveforms is a modified version of the
175   KKS21_GP model (Stähler et al., 2021), in which the upper 80 km is replaced with a radially
176   anisotropic model based on fitting both Rayleigh and Love wave dispersion measurements of
177   S1222a (Beghein et al., 2022) (Fig. S1). The shear attenuation quality factor Q_μ is assumed to be
178   600 in the crust and mantle (e.g., Giardini et al., 2020).
179   The event location and origin time are essential parameters for performing a moment tensor
180   inversion. Here, we fix the origin time to the time reported by MQS and locate the event using
181   the reported back-azimuth. We assume an epicentral distance of 36.0º based on the S – P travel
182   time difference of our preferred velocity model. While uncertainties in the location of the event
183   will introduce uncertainties in the estimations of source properties, we find that our analysis is
184   insensitive to small shifts in source location within the uncertainty bounds of the reported
185   distance and back azimuth of S1222a.

186   Prior to waveform fitting, raw data are instrument-corrected and rotated to the radial (R),
187   transverse (T), and vertical (Z) components. Body wave data are filtered between 3 – 12 s and
188   surface wave data are filtered between 14 – 36 s using a fourth-order nonzero-phase Butterworth
189   filter. The number of cycles for these waves during their propagation from origin is therefore
190   relatively low and about 40, 70 and 30 for P, S, and surface waves (see Table 1), justifying an
191   elastic model with low attenuation. Scattering effects could however still reduce the amplitudes.
192   For each seismic phase, we manually select the windows in which to fit seismic waveforms. For
193   the P-wave, we fit both the Z and R component waveforms in a window starting 10 s before and
194   ending 25 s after the first arriving P energy. For S-waves, we fit waveforms on the T and R
195   components and use a window starting 10 s before and 15 s after the onset of S. The arrival of S
196   on the Z component is unclear, so we omit it from the inversion. Minor arc Rayleigh waveforms
197   are fitted on both Z and R and the Love waveform is fitted on T. Both Rayleigh and Love waves
198   are fitted in 300 s long windows.
199

200   To account for small travel time shifts between observed and predicted data, synthetic
201   waveforms are aligned by cross-correlation prior to calculating the misfit. The maximum
202   allowed travel time shifts are +/- 5 s for P waves, +/- 10 s for S waves and +/- 60 s for Rayleigh
203   and Love waves. To account for uncertainties in the anisotropic velocity model a relative shift
204   between Rayleigh and Love waves of up to +/- 5 s is allowed. This translates to a velocity
205   uncertainty of ~0.02 km/s, which is smaller than the measurement error assumed in the structural
206   inversions of Kim et al., (2022b) and Beghein et al., (2022).
207

208   The best-fitting double-couple solution for each possible depth is found by searching over a grid
209   spanning the range of possible values of strike, dip, and rake, with 60 grid points in each
210   dimension. M_W is varied between 4.2 and 5.0 in increments of 0.05. This search is performed for
211   source depths between 0 – 100 km, with a depth increment of 2 km.
212   For every step in the grid search the misfit χ is calculated using Equation 1 following alignment
213   of observed and synthetic waveforms that maximizes their cross-correlation:
214

215 $$\chi = \sum_{i=1}^{N} w_i \int_0^T \left\| d_i^{obs} - d_i^{syn} \right\|^2 \, \mathrm{d}t$$

216   (Equation 1)
217

218   where d_i^{obs} and d_i^{syn} are the observed and synthetic displacement waveforms in the *i*th window,
219   respectively, *N* is the number of windows, *T* is the window length, and w_i is a weighting factor.
220   Although the choice of phase windows and weights is subjective, it is an important parameter in
221   waveform-based moment tensor inversions. Here, we use two different approaches for weighing
222   body wave and surface wave windows. In the first approach, we apply weights to body waves
223   and surface waves that are inversely proportional to the L2 norm of the observed data vector to
224   ensure that each phase contributes equally to the total misfit. The windows and weights used for
225   the inversion are shown in Table 1. In the second approach, we use the same weights as before,
226   but we amplify the weight in the first 15 s of the P-wave window five times compared to the rest
227   of the window to emphasize the importance of fitting the initial polarity of the P-wave, which
228   may have a smaller amplitude than later arriving phases.
229

Phase	Window start (UTC)	Window end	Window weight	Components	Diff Time (sec) and Q cycle
P	2022-05-04T23:27:34	2022-05-04T23:28:09	45	Z,R	285/38
S	2022-05-04T23:31:15	2022-05-04T23:31:40	8	R,T	501/67
R1	2022-05-04T23:33:57	2022-05-04T23:38:57	1	Z,R	800/32
L1	2022-05-04T23:32:17	2022-05-04T23:37:17	4	T	700/28

230 Table 1. Windows and weights used for inversion. Diff start time is the differential time between middle of the
231 window and quake origin time. Number of Q cycles are computed with central periods of 7.5 and 25 for body and
232 surface waves.
233

3 Results

3.1 Even weighting

236 Figure 2 shows the results of the double couple grid search over source depths of 0 – 100 km, for
237 inversions using even weights for body and surface wave phases. Inversions were performed
238 using both body waves and surface waves together (Fig. 2A), body waves only (Fig. 2B), and
239 surface waves only (Fig. 2C). From here on, we refer to inversions of both body waves and
240 surface waves as BW+SW inversions, and inversions of only body waves or only surface waves
241 as BW or SW inversions, respectively. The lowest misfits of BW+SW inversions are found for
242 sources in the depth range of ~18 – 28 km. In this depth range, the predominant focal mechanism
243 of the best fitting BW+SW solutions is a thrust with a roughly E-W striking fault plane. Thrust
244 fault solutions are mostly found in this depth range for BW and SW inversions, but for BW
245 inversions, a SE-NW striking fault plane is preferred. BW inversions favor events in a similar
246 depth range, although the misfit surface varies more strongly with depth, due to the influence of
247 depth phases. For SW inversions, the misfit varies more smoothly with depth, with the best-
248 fitting solutions found for a source near 26 km. A second minimum in the misfit function near 4
249 km depth suggests that a shallow source cannot be ruled out from SW inversions alone. Events
250 deeper than ~50 km are considered unlikely because the misfit generally increases with
251 increasing depth beyond this range for all inversion types. Below, we outline two plausible
252 scenarios for focal mechanisms at different depths in the crust based on the total misfit and
253 detailed assessment of important aspects of the waveform fits such as body wave first motions.
254

255 The first scenario we consider is a source at 8 km depth (green beachball in Fig. 2A), which is
256 shown in Fig 3A. Although a source depth at 8 km is not in the region of lowest misfit, we
257 include it because its misfit is lower than most other shallow sources, particularly for BW
258 inversions. The best-fitting focal mechanism for the BW+SW grid search is a Mw 4.35 (scalar
259 moment, $M_0 = 4.2 \times 10^{15}$ Nm), predominantly reverse fault, with nodal planes striking either E-W
260 or SE-NW. The P-wave is fitted as the large pulse with an onset near 18 s in the P-wave window.
261 Although the synthetics provide a good match for both the amplitude and wave shape of this
262 signal, the first arriving energy at the P-wave onset time identified by MQS (black arrows, Fig.
263 2) is not fitted. This is because the signal near the MQS-identified P-wave onset has a small
264 amplitude, and thus will have a minor influence on the overall misfit in the P-wave window.
265 Predicted S-waveforms align well with the observed signal with an onset near 10 s in the S-wave
266 window, although amplitudes are slightly underestimated. The predicted Rayleigh wave signal
267 for this moment tensor provides an excellent fit to the observed amplitudes, although the
268 amplitude in the early portion of the signal is underestimated. Synthetic Love waves are in good

269   agreement with both amplitude and phase of the observations. The absolute travel time shift Δt of
270   the Rayleigh wave is 12.0 s and the relative shift between Rayleigh and Love waves Δt_R is 2.15
271   s. Focal mechanisms need not require small absolute travel time shifts of body or surface wave
272   phases because they could reflect uncertainties in source location or errors in the velocity model
273   between their different paths through the interior. However, because our crustal velocity model
274   already includes radial anisotropy that explains well the observed group velocities of minor arc
275   Love and Rayleigh waves, focal mechanisms that imply small relative shifts between Rayleigh
276   and Loves should be preferred.

277

278
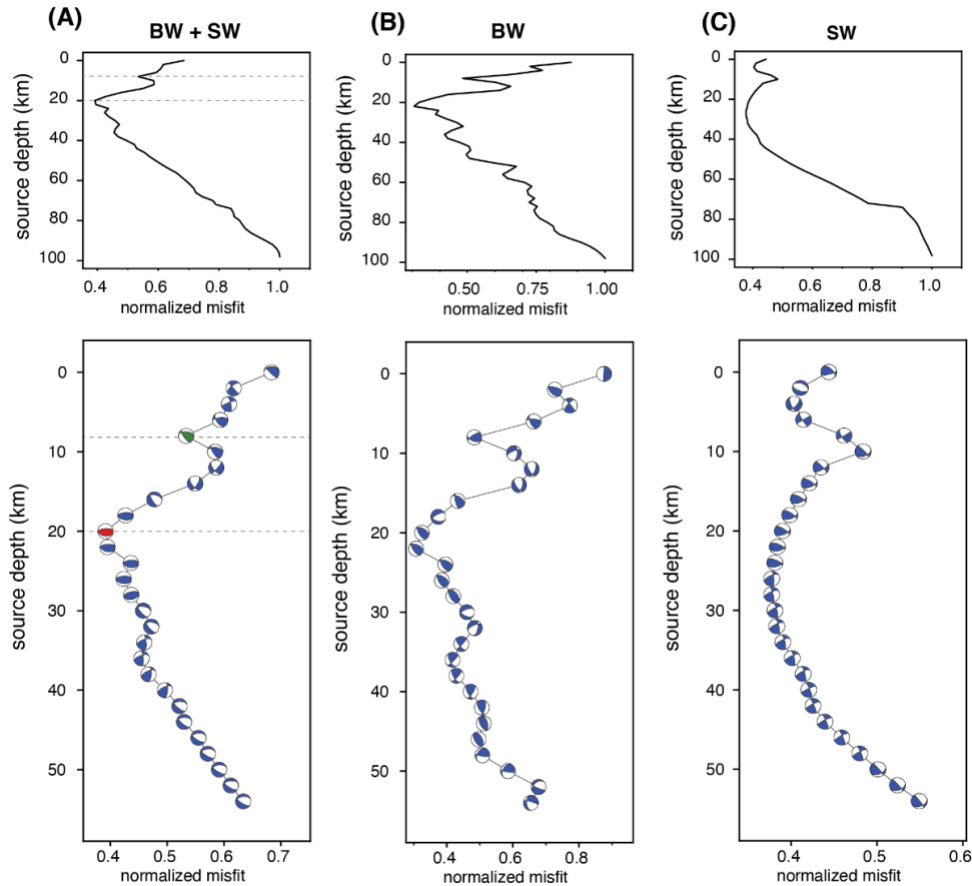
279
280   Figure 2. Inversion misfit for a range of source depths. Panels (A), (B), and (C), show results for
281   BW+SW, BW, and SW inversions, respectively. In each panel, the top figure shows the normalized misfit
282   for the full grid search depth range, and the bottom panel shows the best-fitting moment tensor solutions
283   for source depths shallower than 55 km. The green and red focal mechanisms in (A) represent the two
284   scenarios shown in Figure 3.

285

286   Figure 3B shows the second scenario we consider, which is for a source at 20 km depth (red
287   beachball in Fig. 2). The magnitude of the best-fitting solution Mw 4.4 and the source represents
288   thrusting along an E-W oriented fault plane. The P-wave fit in this scenario is similar to the
289   source at 8 km depth, although the first arriving P-wave energy is a small downward pulse that
290   strongly resembles the observed signal near the MQS identified P-wave time, but with a later
291   onset. This suggests a possible explanation for the P-waveform, in which the small initial pulse
292   identified as the P-wave arrival by MQS (black arrows in Fig. 3) is the direct P which is near

293   nodal takeoff, and the subsequent energy arriving ~8 s later is the depth phase pP (Fig. S2). If
294   this is the case, the timing between P and pP provides a strong constraint on the source depth. An
295   alternative explanation is that the first two arrivals represent two discrete events (e.g., Sita et al.,
296   2022), with a small foreshock occurring ~8 seconds before a larger event. The S-waveform fits
297   also show good agreement with observed amplitudes and satisfy the first motions, and the
298   predicted surface wave fits are similar to the previous case, although the Rayleigh wave phase
299   prediction more clearly matches the observations. Interestingly, if we place this thrust fault
300   solution at the surface, the peak waveform amplitudes of most phases are well fitted, although
301   the small initial P-wave pulse is not reproduced (Fig. S3). Therefore, body waves of S1222a do
302   not seem compatible with a surface source.
303
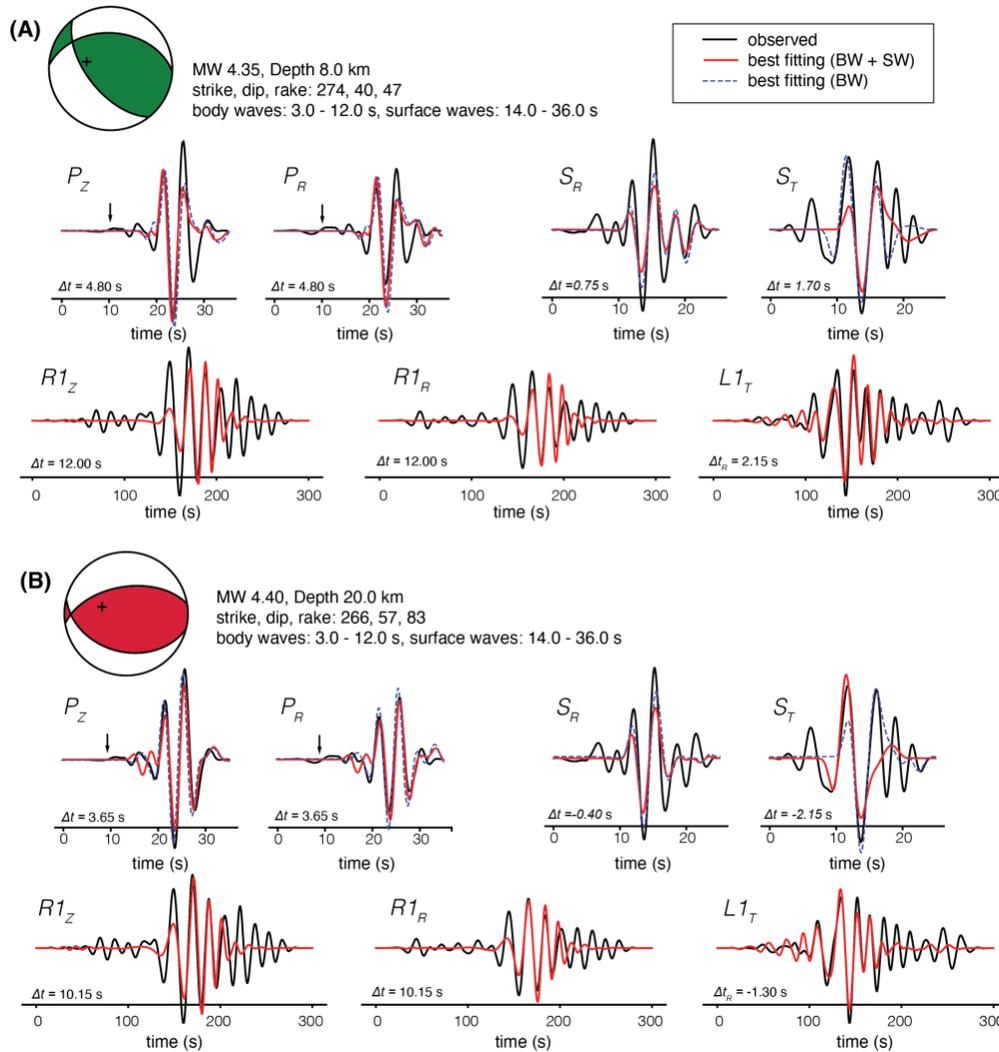
304
305   Figure 3. Best-fitting moment tensors and the corresponding waveform fits shown for source depths at 8
306   km (A), and 22 km (B). Observed waveforms are shown in black and synthetic waveforms of BW+SW
307   and BW inversions are shown in red lines and blue dashed lines respectively. Beachball solutions shown
308   in the top left of each panel represent the best-fitting moment tensor for BW+SW inversions. The +
309   symbol represents the piercing point of the P-wave on the focal-sphere. The black arrows indicate the
310   MQS reported P-wave arrival. The label to the upper left of each waveform indicates the phase
311   (P,S,R1,L1) and component of ground motion (Z,R,T).

312   An additional trend observed is that estimated moment magnitudes are generally lower than the
313   initial MQS estimate of Mw = 4.7, which is based on analysis of the amplitude spectrum. Here,
314   we find moment tensor magnitudes for plausible scenarios range between approximately Mw =
315   4.3 – 4.4 (M_0 = 3.5x10^{15} – 5.0×10^{15} Nm). Additionally, we find a correlation between event
316   depth and estimated magnitude. For example, the mean and standard deviation of the magnitudes
317   of the best fitting moment tensors is Mw = 4.42 +/- 0.16 (M_0 between 3.1x10^{15} – 9.3×10^{15} Nm)
318   for source depths between 0 – 50 km, and Mw = 4.71 +/- 0.08 (M_0 between 1.1x10^{16} – 1.92×10^{16}
319   Nm) for source depths between 50 – 100 km. Thus, a deeper source implies a larger magnitude,
320   although deeper events are less likely due to their larger misfit values.
321

322   **3.2 Heavily weighted P-wave first arrival**

323
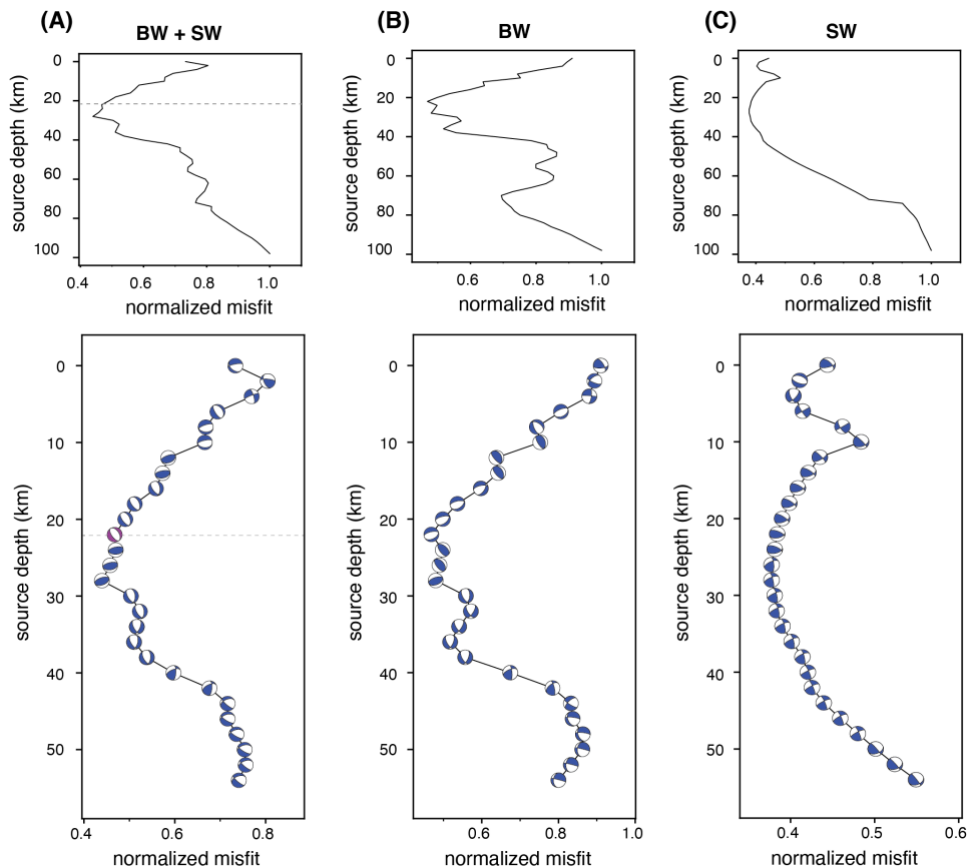
324
325   Figure 4. Same as Fig. 2, but for inversions with a higher weight applied to the early part of the P-wave
326   window
327

328   The potential importance of inversions that emphasize fitting the relatively low amplitude, early
329   part of the P-wave is illustrated in Figure 4. When the first 15 s of the P-wave window are up-
330   weighted by a factor of 5, the best-fitting solutions of BW+SW inversions are found in a similar
331   depth range as previous inversions, but the focal mechanism solutions are different (Fig. 4A).
332   For sources near 20 km depth, where evenly weighted inversions found E-W striking thrust fault
333   solutions, a SE-NW striking normal fault provides the best solution. The waveform fits for the

best-fitting normal fault solution at 22 km depth (purple beachball in Fig. 4A), are shown in Fig.
5A. In this case, both the low amplitude signal near the MQS P-wave pick and the larger
subsequent arrivals are well fitted (correlation coefficient 0.91). Overall, surface wave fits are
similar to those shown in Fig 3B (thrust fault solution at 20 km depth), although the early
arriving long period Rayleigh wave signal appears to be reproduced better. The lowest misfit
value is found for a source at 28 km depth, where the best-fitting solution is an ENE-WSW
striking thrust fault (Fig. S4).
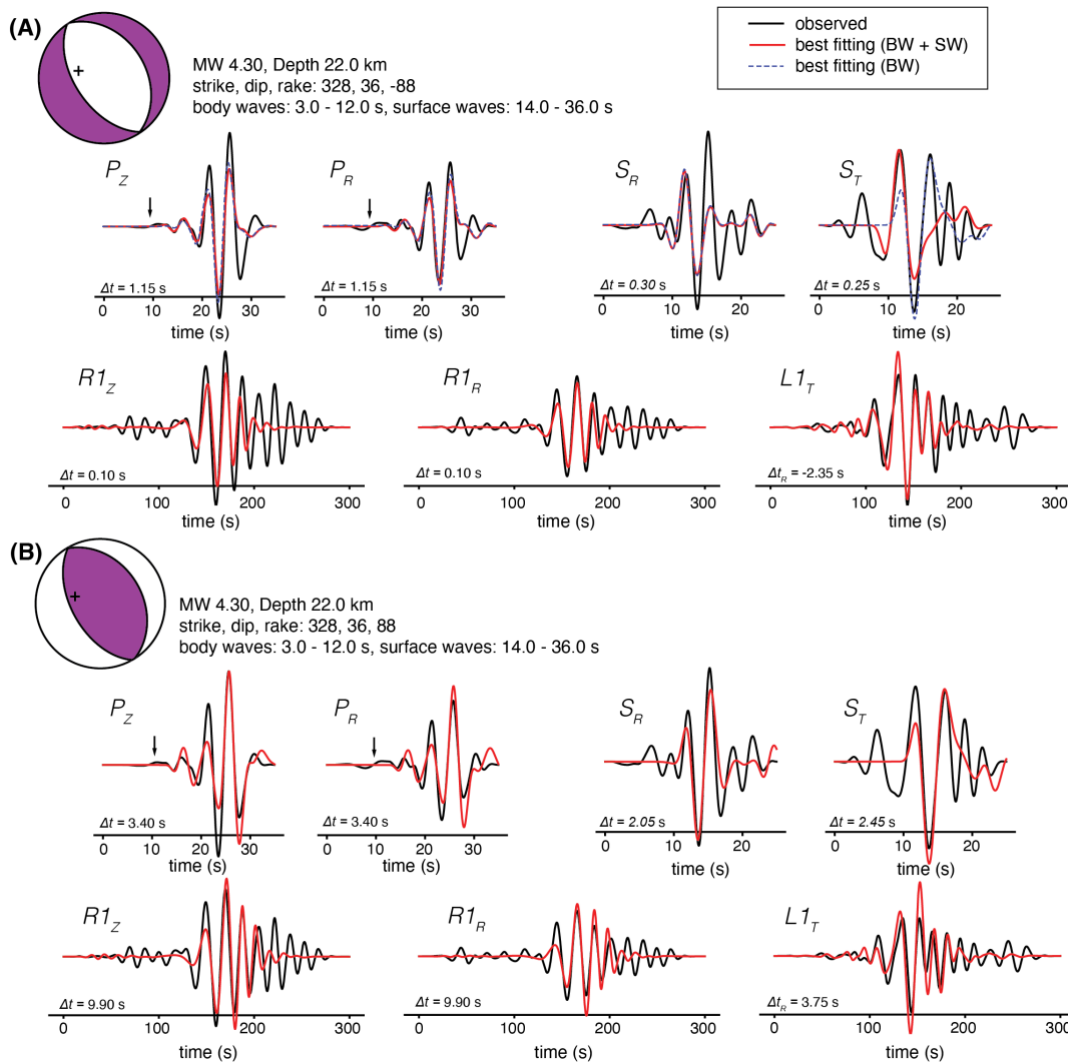
Figure 5. (A) Same as Fig. 3, but a high weight was applied to the early portion of the P-wave window. The
best-fitting moment tensor and waveform fits are shown for a source at 22 km depth (purple beachball
shown in Fig. 4A). (B) Predicted waveforms for a reverse fault with the same strike and dip as the focal
mechanism shown in panel (A).

Understanding the uncertainties of moment tensor inversions is important for making robust
inferences about crustal faulting mechanisms. Here, we take a grid search approach that allows
assessment of the misfit over the full range of possible double couple moment tensors. Figure 6
shows cross sections through the 3D misfit volume for a source at 22 km depth, for an inversion
emphasizing the early part of the P-wave window. The structure of the misfit volumes is

353 complex with multiple local minima, some of which may not be significantly larger in value than
354 the global minimum. For example, although the global minimum of the inversion for a source at
355 22 km depth suggests a normal fault solution (black circles in Fig 6), the misfit slice in Fig 6C is
356 almost symmetrical, indicating that a thrust fault solution on a similarly oriented fault plane can
357 achieve a similar data fit. Fig. 5B shows waveform fits for a thrust fault solution assuming a
358 source at 22 km depth and the same fault plane orientation as the best-fitting normal fault
359 solution.

360
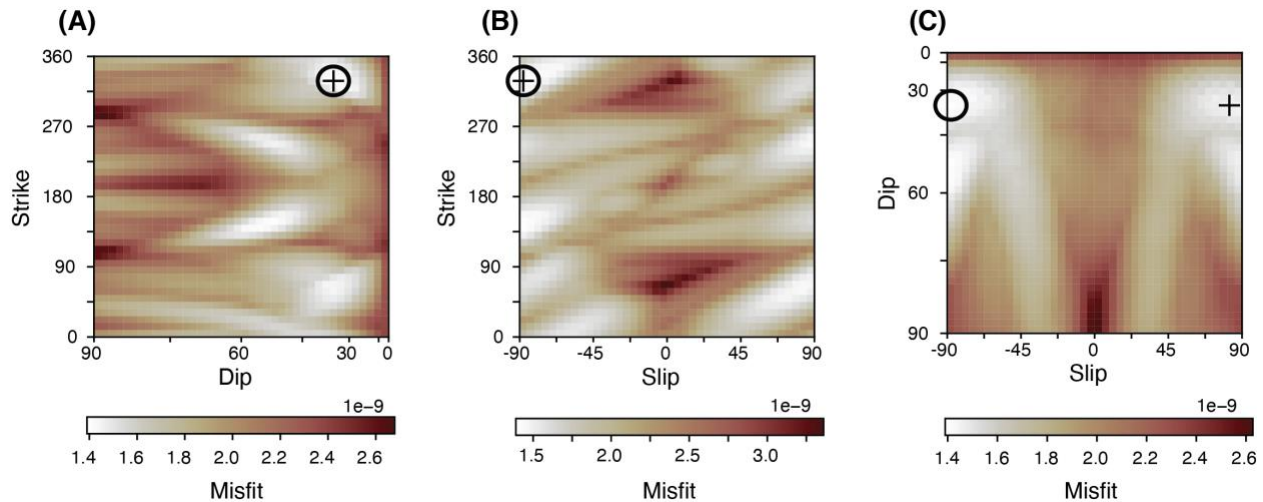
361
362 Figure 6. Cross sections through the 3D misfit volume of a grid search using a source depth of 22 km.
363 The early portion of the P-wave window was more heavily weighted in the misfit function. The black
364 circles show the location of the best-fitting moment tensor solution (Fig. 5A), and the + symbol shows the
365 location of the reverse fault solution shown in Fig. 5B.

4 Discussion

367 Without definitive detection of body wave depth phases the source depth of S1222a is uncertain.
368 Giardini et al., (2020) proposed that LF events likely originate in the uppermost mantle, which
369 could explain the lack of high frequencies that would be attenuated away in the mantle. Since
370 then, other observed marsquakes have challenged this paradigm. For example, high frequency
371 energy (> 5 Hz) has been observed from teleseismically detected impacts (Posiolova et al., 2022;
372 Kim et al., 2022a) with mantle traversing body waves.

373
374 The signal duration may provide an additional depth discriminant because shallow events are
375 likely to produce longer coda due to extensive scattering in the near-surface (e.g., van Driel et
376 al., 2021; Karakostas 2022). S1222a has one of the longest durations of any recorded marsquake,
377 above 8 hours for the multiple orbit surface waves and about an hour in the body wave coda (see
378 Fig. 1), which suggests a shallow origin. Without more precise knowledge of the subsurface
379 structure along the path, this remains fairly qualitative speculation. For Cerberus Fossae events,
380 the corner frequency may be indicative of source depth because the lower corner frequencies of
381 LF events compared to HF events are thought to result from their origin in deeper, warmer,
382 structurally weaker zones (Stähler et al., 2022). Similarly, shallow moonquakes exhibit higher
383 corner frequencies than deep moonquakes, likely indicating a high-stress drop (Oberst, 1987).
384 Outside of Cerberus Fossae, LF events generally have higher corner frequencies, making the
385 relationship between source depth and corner frequency less clear. The high corner frequency

386   observed for S1222a (~ 4 Hz, see Kawamura et al. 2022) could result from a combination of high
387   stress drop and a cold, weakly attenuating lithosphere.

389   The structural model used to generate Green's functions is a key component of moment tensor
390   inversions. Ideally, 3D models that account for structural variations near the source and receiver
391   would be used so that reflected and converted body wave phases can be accurately modeled.
392   However, in this study we are limited to one-dimensional (1D) structural models owing to the
393   lack of accurate knowledge of along-path variations in structure that are necessary to accurately
394   simulate high frequency waveforms. Indeed, moment tensor inversions on Earth are often limited
395   to lower frequencies when 1D structural models are used to compute Green's functions (e.g.
396   Dreger and Helmberger, 1993). The structural model used here is based on fitting fundamental
397   mode dispersion of Rayleigh and Love waves (Beghein et al., 2022), although our results do not
398   change significantly if we use the model of Kim et al., (2022b), which fits both fundamental
399   mode and overtone data (Fig. S5). Although using models constructed from surface wave
400   dispersion enables accurate fitting of Rayleigh and Love waveforms, the model does not
401   incorporate constraints on crustal layering below InSight. A structural model based on joint
402   inversion of surface wave dispersion and receiver functions could potentially improve moment
403   tensor estimations because waveform predictions would include converted and reflected body
404   wave phases from discontinuities below InSight. Near-source scattering, however, would remain
405   unaccounted for.

407   The likely source region of S1222a, to the northwest of Apollinaris Mons, lies near the martian
408   hemispheric dichotomy boundary which divides the highly cratered southern highlands and less
409   cratered northern lowlands. In this region, Knapmeyer et al., (2006) inferred the presence of
410   relatively young (< 500 Ma) compressional faults based on wrinkle ridge structures that are
411   likely to be the surface expression of blind thrusts at depth. The orientation of these faults is
412   predominantly N-S, which is inconsistent with the best-fitting thrust fault solutions at most
413   crustal depths, although this orientation cannot be ruled out (e.g., Fig 6). If S1222a indeed
414   resulted from compressional faulting on one of these blind thrusts it would represent the first
415   observation of a tectonically active wrinkle ridge system, and only the second confirmed
416   seismically active tectonic feature on Mars beside the Cerberus Fossae system.

418   The majority of reverse faulting solutions represent crustal shortening along E-W or NE-SW
419   oriented fault planes, which is roughly parallel to the outline of the dichotomy boundary. Jacob
420   et al. (2022) inferred a similar focal mechanism for the marsquake S0784a, which likely occurred
421   to the southeast of InSight near the dichotomy boundary. They suggest that S0784a resulted from
422   motion along a fault that originally accommodated subsidence of the northern lowlands but has
423   since been reactivated in a compressional regime due to planetary contraction. Although events
424   S0784a and S1222a have different source locations, it is plausible that they represent the same
425   tectonic environment.

427   Over the course of the InSight mission, the majority of significant marsquakes have been related
428   to extensional tectonics in the Cerberus Fossae system, and compressional faulting due to
429   planetary contraction did not appear associated with the observed seismic activity. Stähler et al.,
430   (2022) estimate that the Cerberus Fossae events account for an annual seismic moment release
431   of 1.4-5.6×10^{15} Nm/yr, or over half of seismic moment release in the InSight hemisphere. The

432 estimated scalar moment of S1222a is $3.5\times10^{15} - 5.0\times10^{15}$ Nm, suggesting that this event alone
433 accounts for a large fraction of the annual seismic budget of Mars. If S1222a did result from
434 compressional faulting, it may suggest that planetary thermal contraction is an ongoing source of
435 seismicity on Mars, as was expected prior to the arrival of InSight, although it is questionable
436 whether planetary cooling could generate such a large event. Thus, resolving the ambiguity in the
437 focal mechanism of S1222a remains an important goal for understanding the nature of active
438 tectonic deformation on Mars.

5 Conclusions

440 Based on waveform fits from P, S, Rayleigh, and Love wave phases, we estimated the source
441 properties and focal mechanism of S1222a, the largest marsquake recorded during the InSight
442 mission. Our approach, which included minimizing the L2 misfit between broadband
443 observations and synthetic seismograms via a grid search allowed us to estimate the best-fitting
444 magnitude and focal mechanism, as well as understand the uncertainties on the source
445 parameters. We find that S1222a resulted from either reverse faulting or normal faulting along an
446 E-W to SE-NW oriented fault plane at moderate depth in the crust (< 50 km). Potential depth
447 phases suggest a source depth near 20 km, but the complexity of the signal does not rule out a
448 shallower source at 5-10 km depth. The estimated moment magnitude of S1222a is Mw = 4.3 –
449 4.4 (M_0 between $3.5\times10^{15} - 5.0\times10^{15}$ Nm), lower than initially determined by MQS. The most
450 likely fault plane orientation is roughly parallel to the dichotomy boundary, potentially indicating
451 either extension along boundary faults accommodating subsidence of the northern lowlands, or
452 reactivation of fault systems in a compressional regime (e.g., Jacob et al., 2022). We cannot rule
453 out the possibility that S1222a occurred on a blind thrust fault associated with wrinkle ridge
454 deformation. Future work may be able to provide tighter constraints on the focal mechanism of
455 S1222a (and other marsquakes) if improved structural models of Mars become available, or if
456 additional seismic phases are clearly identified.

Open Research

471 Seismic data from the InSight mission is openly available from IRIS Data Management Center
472 (https://ds.iris.edu/ds/nodes/dmc/), the InSight SEIS Data Service at IPGP (https://www.seis-

insight.eu/en/science/seis-data/seis-data-description), and the NASA Planetary Data System (https://pds-geosciences.wustl.edu/missions/insight/).

References

Arvidsson, R., & Ekström, G. (1998). Global CMT analysis of moderate earthquakes, Mw≧ 4.5, using intermediate-period surface waves. *Bulletin of the Seismological Society of America*, 88(4), 1003-1013.

Banerdt, W. B., Smrekar, S. E., Banfield, D., Giardini, D., Golombek, M., Johnson, C. L., ... & Wieczorek, M. (2020). Initial results from the InSight mission on Mars. *Nature Geoscience*, 13(3), 183-189.

Basham, P. W., & Ellis, R. M. (1969). The composition of P codas using magnetic tape seismograms. *Bulletin of the Seismological Society of America*, 59(2), 473-486.

Beghein, C., Li, J., Weidner, E., Maguire, R., Wookey, J., Lekić, V., ... & Banerdt, W.B. (2022). Crustal Anisotropy in the Martian lowlands from surface waves. *Geophysical Research Letters*, 49(24), e2022GL101508.

Böse, M., Stähler, S.C., Deichmann, N., … & Banerdt, W.B., (2021). Magnitude Scales for Marsquakes Calibrated from InSight Data. *Bulletin of the Seismological Society of America*. https://doi.org/10.1785/0120210045

Brinkman, N., Stähler, S. C., Giardini, D., Schmelzbach, C., Khan, A., Jacob, A., ... & Banerdt, W. B. (2021). First focal mechanisms of marsquakes. *Journal of Geophysical Research: Planets*, 126(4), e2020JE006546.

Brumbaugh, D. S. (1979). Classical focal mechanism techniques for body waves. *Geophysical Surveys*, 3(4), 297-329.

Ceylan, S., Clinton, J. F., Giardini, D., Stähler, S. C., Horleston, A., Kawamura, T., ... & Banerdt, W. B. (2022). The marsquake catalogue from InSight, sols 0–1011. *Physics of the Earth and Planetary Interiors*, 333, 106943.

Dreger, D. S., & Helmberger, D. V. (1993). Determination of source parameters at regional distances with three-component sparse network data. *Journal of Geophysical Research: Solid Earth*, 98(B5), 8107-8125.

Dreger, D. S., Gritto, R., & Nelson, O. (2021). Path calibration of the democratic People's Republic of Korea 3 September 2017 nuclear test. *Seismological Society of America*, 92(6), 3375-3385.

Durán, C., Khan, A., Ceylan, S., Zenhäusern, G., Staehler, S., Clinton, J. F., & Giardini, D. (2022a). Seismology on Mars: An analysis of direct, reflected, and converted seismic body waves with implications for interior structure. *Physics of the Earth and Planetary Interiors*, 325, 106851.

Durán, C., Khan, A., Ceylan, S., Charalambous, C., Kim, D., Drilleau, M., ... & Giardini, D. (2022b). Observation of a Core-Diffracted P-Wave From a Farside Impact With Implications for the Lower-Mantle Structure of Mars. *Geophysical Research Letters*, 49(21), e2022GL100887.

Dziewonski, A. M., Chou, T. A., & Woodhouse, J. H. (1981). Determination of earthquake source parameters from waveform data for studies of global and regional seismicity. Journal of *Geophysical Research: Solid Earth*, 86(B4), 2825-2852.

Dziewonski, A. M., & Woodhouse, J. H. (1983). An experiment in systematic study of global seismicity: Centroid-moment tensor solutions for 201 moderate and large earthquakes of 1981. *Journal of Geophysical Research: Solid Earth*, 88(B4), 3247-3271.

Ekström, G., Nettles, M., & Dziewoński, A. M. (2012). The global CMT project 2004–2010: Centroid-moment tensors for 13,017 earthquakes. *Physics of the Earth and Planetary Interiors*, 200, 1-9.

Giardini, D., Lognonné, P., Banerdt, W. B., Pike, W. T., Christensen, U., Ceylan, S., ... & Yana, C. (2020). The seismicity of Mars. *Nature Geoscience*, 13(3), 205-212.

Huang, Q., Schmerr, N. C., King, S. D., Kim, D., Rivoldini, A., Plesa, A. C., ... & Banerdt, W. B. (2022). Seismic detection of a deep mantle discontinuity within Mars by InSight. *Proceedings of the National Academy of Sciences*, 119(42), e2204474119.

InSight Marsquake Service (2023). Mars Seismic Catalogue, InSight Mission; V13 2023-01-01. ETHZ, IPGP, JPL, ICL, Univ. Bristol. https://doi.org/10.12686/a19

InSight Mars SEIS Data Service. (2019). Seis raw data, insight mission. IPGP, JPL, CNES, ETHZ, ICL, MPS, ISAE-Supaero, LPG, MFSC. Retrieved from https:// datacenter.ipgp.fr/networks/detail/XB_2016/ doi: 10.18715/SEIS.INSIGHT .XB_2016

Jacob, A., Plasman, M., Perrin, C., Fuji, N., Lognonné, P., Xu, Z., ... & Banerdt, W. B. (2022). Seismic sources of InSight marsquakes and seismotectonic context of Elysium Planitia, Mars. *Tectonophysics*, 229434.

Karakostas, F., Schmerr, N., Maguire, R., Huang, Q., Kim, D., Lekic, V., ... & Banerdt, B. (2021). Scattering Attenuation of the Martian Interior through Coda-Wave Analysis. *Bulletin of the Seismological Society of America*, 111(6), 3035-3054.

Kawamura, T., Clinton, J. F., Zenhäusern, G., Ceylan, S., Horleston, A. C., Dahmen, N. L., ... & Banerdt, W. B. (2022). S1222a-the largest Marsquake detected by InSight. *Geophysical Research Letters*, e2022GL101543.

Khan, A., Ceylan, S., van Driel, M., Giardini, D., Lognonné, P., Samuel, H., ... & Banerdt, W. B. (2021). Upper mantle structure of Mars from InSight seismic data. *Science*, 373(6553), 434-438.

Khan, A., Sossi, P. A., Liebske, C., Rivoldini, A., & Giardini, D. (2022). Geophysical and cosmochemical evidence for a volatile-rich Mars. *Earth and Planetary Science Letters*, 578, 117330.

Kim, D., Lekić, V., Irving, J. C.E., Schmerr, N., Knapmeyer-Endrun, B., Joshi, R., ... & Banerdt, W. B. (2021a). Improving constraints on planetary interiors with PPs receiver functions. *Journal of Geophysical Research: Planets*, 126(11), e2021JE006983.

Kim, D., Davis, P., Lekić, V., Maguire, R., Compaire, N., Schimmel, M., ... & Banerdt, W. B. (2021b). Potential pitfalls in the analysis and structural interpretation of seismic data from the Mars InSight mission. *Bulletin of the Seismological Society of America*, 111(6), 2982-3002.

Kim, D., Banerdt, W. B., Ceylan, S., Giardini, D., Lekić, V., Lognonné, P., ... & Panning, M. P. (2022a). Surface waves and crustal structure on Mars. *Science*, 378(6618), 417-421.

Kim, D., Stähler, S. C., Ceylan, S., Lekić, V., Maguire, R., Zenhäusern, G., ... & Banerdt, W. B. (2022b). Structure Along the Martian Dichotomy Constrained by Rayleigh and Love Waves and their Overtones. *Geophysical Research Letter*s, e2022GL101666.

Knapmeyer, M, Oberst, J., Hauber, E., Wählisch, M., Deuchler, C., and Wagner, R., Working Models for Spatial Distribution and Level of Mars' Seismicity (2006). *Journal of Geophysical Research E: Planet*s 111(11), 1–23. https://doi.org/10.1029/2006JE002708.

Knapmeyer-Endrun, B., Panning, M. P., Bissig, F., Joshi, R., Khan, A., Kim, D., ... & Banerdt, W. B. (2021). Thickness and structure of the martian crust from InSight seismic data. *Science*, 373(6553), 438-443.

Langston, C. A., & Helmberger, D. V. (1975). A procedure for modelling shallow dislocation sources. *Geophysical Journal International*, 42(1), 117-130.

Li, J., Beghein, C., Davis, P., Wieczorek, M. A., Mclennan, S. M., Kim, D., ... & Banerdt, W. B. (2022a). Crustal Structure Constraints from the Detection of the SsPp Phase on Mars. *Earth and Space Science*, e2022EA002416.

Li, J., Beghein, C., Wookey, J., Davis, P., Lognonné, P., Schimmel, M., Stutzmann, E., Golombek, M., Montagner, J.-P., and Banerdt, W. (2022b), Evidence for Crustal Seismic Anisotropy at the InSight Lander Site, *Earth and Planetary Science Letters*., 593, 117654, doi: 10.1016/j.epsl.2022.117654

Li., J., Beghein, C., Lognonné, P., McLennan, S., Wieczorek, M.A., Panning, M., Knapmeyer-Endrun, B., Davis, P., and Banerdt, W. (2022c), Different Martian Crustal Seismic Velocities across the Dichotomy Boundary from Multi-Orbiting Surface Waves, *Geophysical Research Letters*, 50, 1, doi:10.1029/2022GL101243

Li, J., Beghein, C., McLennan, S.M., Lognonné, P., Horleston, A.C., Charalambous, C., Huang, Q., Zenhäusern, G., Bozdag, E., Pike, T. W., Golombek M., Lekić, V., Lognonné, P., & Banerdt, W. (2022d), Second Seismic Anchor Point of the Martian Crustal Structure Away From the InSight Landing Site, *Nature Communications*, 13, 1, doi:10.1038/s41467-022-35662-y

Lognonné, P., Banerdt, W. B., Giardini, D., Pike, W. T., Christensen, U., Laudet, P., ... & Wookey, J. (2019). SEIS: Insight's seismic experiment for internal structure of Mars. *Space Science Reviews*, *215*, 1-170.

Lognonné, P., Banerdt, W. B., Pike, W. T., Giardini, D., Christensen, U., Garcia, R. F., ... & Zweifel, P. (2020). Constraints on the shallow elastic and anelastic structure of Mars from InSight seismic data. *Nature Geoscience*, 13(3), 213-220.

Menina, S., Margerin, L., Kawamura, T., Lognonné, P., Marti, J., Drilleau, M., ... & Banerdt, W. B. (2021). Energy envelope and attenuation characteristics of high-frequency (HF) and very-high-frequency (VF) Martian events. *Bulletin of the Seismological Society of America*, 111(6), 3016-3034.

Nissen-Meyer, T., van Driel, M., Stähler, S.C., Hosseini, K., Hempel, S., Auer, L., Colombi, A. and Fournier, A., 2014. AxiSEM: broadband 3-D seismic wavefields in axisymmetric media. *Solid Earth*, 5(1), pp.425-445.

592   Oberst, J. (1987). Unusually high stress drops associated with shallow moonquakes. *Journal of*
593   *Geophysical Research: Solid Earth*, 92(B2), 1397-1405.

594   Posiolova, L. V., Lognonné, P., Banerdt, W. B., Clinton, J., Collins, G. S., Kawamura, T., ... &
595   Zenhäusern, G. (2022). Largest recent impact craters on Mars: Orbital imaging and surface
596   seismic co-investigation. *Science*, 378(6618), 412-417.

597   Sita, M., & van der Lee, S. (2022). Potential volcano-tectonic origins and faulting mechanisms of
598   three low-frequency Marsquakes detected by a single InSight seismometer. *Journal of*
599   *Geophysical Research: Planets*, e2022JE007309.

600   Solomon, S.C., Anderson, D.L., Banerdt, W.B., Butler, R.G., Davis, P.M., Duennebier, F.K.,
601   Nakamura, Y., Okal, E.A. and Phillips, R.J., 1991. Scientific rationale and requirements for a
602   global seismic network on Mars. LPI Tech. Rept. 91-02. Lunar and Planetary Inst., Houston, TX.

603   Stähler, S.C., Mittelholz, A., Perrin, C., Kawamura, T., Kim, D., Knapmeyer, M., Zenhäusern,
604   G., Clinton, J., Giardini, D., Lognonné, P. and Banerdt, W.B., 2022. Tectonics of Cerberus
605   Fossae unveiled by marsquakes. *Nature Astronomy*, **6**, 1376–1386.

606   Stähler, S. C., Khan, A., Banerdt, W. B., Lognonné, P., Giardini, D., Ceylan, S., ... & Smrekar, S.
607   E. (2021). Seismic detection of the martian core. *Science*, 373(6553), 443-448.

608   Tsai, Y. B., & Aki, K. (1970). Precise focal depth determination from amplitude spectra of
609   surface waves. *Journal of Geophysical Research*, 75(29), 5729-5744.

610   van Driel, M., Krischer, L., Stähler, S. C., Hosseini, K., & Nissen-Meyer, T. (2015). Instaseis:
611   Instant global seismograms based on a broadband waveform database. *Solid Earth*, 6(2), 701-
612   717.

613   van Driel, M., Ceylan, S., Clinton, J. F., Giardini, D., Horleston, A., Margerin, L., ... & Banerdt,
614   W. B. (2021). High-frequency seismic events on Mars observed by InSight. *Journal of*
615   *Geophysical Research: Planets*, 126(2), e2020JE006670.